ACS OMEGA

Open Access



http://pubs.acs.org/journal/acsodf

Article

# Innovative Preparation of Cellulose-Mediated Silver Nanoparticles for Multipurpose Applications: Experiment and Molecular Docking Studies

Arularasu M. Visagamani,* Durairaj Shanthi, Appusamy Muthukrishnaraj, Babu Venkatadri, J. Irshad Ahamed, and Kasinathan Kaviyarasu*

Cite This: *ACS Omega* 2023, 8, 38860−38870

Read Online

ACCESS | Metrics & More | Article Recommendations | Supporting Information

**ABSTRACT:** In recent years, inorganic metal nanoparticle fabrication by extraction of a different part of the plant has been gaining more importance. In this research, cellulose-mediated Ag nanoparticles (cellulose/Ag NPs) with excellent antibacterial and antioxidant properties and photocatalytic activity have been synthesized by the microwave-assisted hydrothermal method. This method is a green, simple, and low-cost method that does not use any other capping or reducing agents. X-ray diffraction (XRD), Fourier transform infrared (FTIR), field emission scanning microscopy (FESEM), transmission electron microscopy (TEM), energy-dispersive X-ray (EDX), and UV−visible spectroscopic techniques were used to investigate the structure, morphology, as well as components of the generated cellulose/Ag NPs. In fact, XRD results confirm the formation of the face-centered cubic phase of Ag nanoparticles, while the FTIR spectra showed that the synergy of carbohydrates and proteins is responsible for the formation of cellulose/Ag NPs by the green method. It was found that the green-synthesized silver nanoparticles showed good crystallinity and a size range of about 20−30 nm. The morphology results showed that cellulose has a cavity-like structure and the green-synthesized Ag NPs were dispersed throughout the cellulose polymer matrix. In comparison to cellulose/Ag NPs and Ag nanoparticles, cellulose/Ag NPs demonstrated excellent antibacterial activity, *Proteus mirabilis* (MTCC 1771) possessed a maximum inhibition zone of 18.81.5 mm at 2.5 g/mL, and *Staphylococcus aureus* (MTTC 3615) had a minimum inhibition zone of 11.30.5 mm at 0.5 g/mL. Furthermore, cellulose/Ag NPs also exhibited a significant radical scavenging property against the DDPH free radical, and there was a higher degradation efficiency compared to pure Ag NPs against Rhodamine B as 97.38% removal was achieved. Notably, cellulose/Ag NPs remarkably promoted the transfer and separation of photogenerated electron−hole ($e^-/h^+$) pairs, thereby offering prospective application of the photodegradation efficiency for Rhodamine B (RhB) as well as antibacterial applications. With the findings from this study, we could develop efficient and environmentally friendly cellulose/Ag nanoparticles using low-cost, environmentally friendly materials, making them suitable for industrial and technological applications.

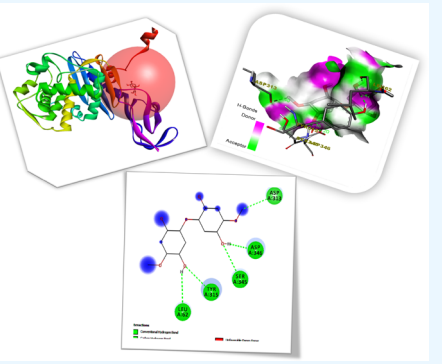

## 1. INTRODUCTION

The research community has been faced with the challenging task of developing powerful, novel, and cost-effective antibiotics in response to the growing menace of bacterial resistance.[1] The eradication of harmful microorganisms' adhesion, contamination, colonization, and persistence on surfaces by viruses and bacteria is crucial for safeguarding public health and society.[2] A number of materials with potent antibacterial activity have been developed to kill microbes, such as organic antibacterial agents and inorganic materials.[3,4] Organic-based antibiotics are sensitive to high-pressure and -temperature processing conditions; therefore, recently inorganic nanomaterial-based antibiotics have become a hot research interest for drug design and development.[5,6] Inorganic antibacterial agents are superior to antibacterial materials toward viruses, yeasts, fungi, and bacteria because of their long shelf life and good stability at high pressure and temperature.[7] Metallic and metal oxide nanoparticles, such as copper, gold, silver, zinc oxide, titanium dioxide, copper oxide, as well as magnesium oxide, exhibit a diverse array of antibacterial compounds.[8,9] Among these, silver nanoparticles (Ag NPs) are well-known antibacterial as well as wound-healing substances.[10,11] Furthermore, Ag NPs release silver ions ($Ag^+$), which inhibit respiratory enzymes responsible for reactive oxygen species (ROS) production; therefore, Ag NPs are widely used in medicines, cleaning agents, food, as well as consumer

Received: April 11, 2023
Accepted: May 29, 2023
Published: October 10, 2023

products.[12] However, pure Ag NPs are used in a limited manner in direct antibacterial application and wastewater treatment due to their poor antibacterial activity, high cost, and low electron−hole pair recombination. In the conventional process, silver ions are reduced by various methods, such as the high-temperature process, using capping agents (gelatine), and reducing the amount of silver ions in the liquid medium (sodium borohydride). Recently, researchers have focused on developing green synthesis of Ag NPs employing plant extracts as natural reducing and stabilizing agents for Ag NPs.[13]

*Ipomoea quamoclit* is a member of the *Convolvulaceae* family, also known as *Quamoclit pinnata*, and is found mostly in Asia, North America, and Europe. *I. quamoclit*, ayurvedic and traditional medicine depend on this plant, also known as Indian pink, cardinal vine, and star glory. *I. quamoclit* stems and leaves contain trace levels of cyanogenetic glycosides, including alkaloids. To alleviate bleeding piles and carbuncles, plant leaves are utilized. The plant *I. quamoclit* has several therapeutic qualities, including anticancer, antidiabetic, antibacterial, and antioxidant properties.

Cellulose is the most abundant, eco-friendly, renewable, biodegradable, and widespread natural biopolymer on earth.[14−16] Cellulose also has a low thermal expansion, high modulus, good mechanical properties, hydrophilicity, piezoelectricity, and low density. Cellulose is a linear repeated unit containing 1,4-$\beta$ glucan chains, which is covalently linked to one of the neighboring glucose rings C1 and C4, which possess strong inter- and intramolecular hydrogen bonds.[17,18] This makes cellulose nondissolvable in most common organic solvents and water. Cellulose-based composites are used for textile, optical, biomedical, and coating technology.[19,20] In recent years, cellulose has become a very promising material for sustainable development, especially associated with the nanoscience technique. Incorporation of silver nanoparticles into cellulose polymers provides the following advantages for antibacterial and photocatalytic activity: (i) nontoxic and biocompatible material due to naturally available polymers; (ii) cellulose acts as a natural reducing and a stabilizing agent; and (iii) cellulose is easily available.

Here, we propose that the cellulose/Ag NPs (1:1 ratio) were synthesized by a green and microwave-assisted hydrothermal method having a good crystalline nature with a tunable morphology, produced from organic−inorganic hybrid cellulose/Ag NPs, as well as an increased antibacterial potential against human pathogens (Gram-positive bacteria and Gram-negative bacteria). Also, cellulose/Ag NPs and Ag NPs were examined for their photocatalytic and antioxidant properties in the current study's investigation of dye degradation. However, this study offers a low-cost and environmentally friendly technique of precipitating multifunctional cellulose/Ag NPs. To the best of the authors' knowledge, this is the only study to investigate molecular docking studies for cellulose/Ag NPs as well as the interfacial contact.

## 2. EXPERIMENTAL SECTION

**2.1. Preparation of *I. quamoclit* L. Leaf Extract.** To eliminate dust particles, *I. quamoclit* was gathered locally and rinsed with sterile distilled water. The clean leaves were pulverized using an electric grinder after being chopped into tiny pieces. Following that, 10 g of powder was mixed with 100 ml of deionized water, as well as the solution was boiled in a water bath at 100 °C for 30 min. Lastly, the extract was filtered and stored in an argon environment for future use.

**2.2. Synthesis of Silver Nanoparticles (Ag NPs).** Initially, a 1 mM $AgNO_3$ solution was prepared; next, at room temperature, 25 mL of leaf extract was gently mixed with an aqueous $AgNO_3$ solution, which was then added while being constantly stirred. Second, the combined solution was kept in the HPCM apparatus for 20 min (Barnstead Thermolyne, SP46925) at 400 °C. The nanoparticles were centrifuged at 5000 rpm for about 15 min. The synthesized Ag NPs were suspended, rinsed with deionized water, and then fired at 100 °C for 1 h before being ground and characterized.

**2.3. Preparation of Cellulose/Ag Composites.** The synthesis of cellulose/Ag composite samples by the microwave-assisted hydrothermal method was carried out as follows. 1.6 g of cellulose was distributed in a 100 mL mixture solution including 75 mL of deionized water, 5 mL of TEMPO, 10 mL of $NH_4OH$, 6 mL of *N*,*N*-dimethylacetamide, and 4 mL of urea, and further sonication was performed for 1 h to result in the formation of a homogeneous solution. Then, 1.07 g of green-synthesized Ag NPs was dissolved in deionized water, and the resulting solution was magnetically stirred for 1 h. After stirring for 1 h, each precursor was transferred to a microwave oven and heated at 900 Watts for 15 min. Lastly, the cellulose/Ag NPs were rinsed with deionized water as well as ethanol until completely neutralized and then dried in an oven at 500 °C for about 3 h to increase crystallinity.

**2.4. Characterization Studies.** The crystalline nature of nanoparticles was investigated by X-ray diffraction (XRD) patterns obtained using Cu K radiation (1.5406 Å) on the Bruker D8 Advance (Germany) at an acceleration voltage of 40 kV and diffraction angle 2$\theta$ range of 10−80°. The presence of silver nanoparticles and their interaction with cellulose matrix synthesized cellulose/Ag NPs were studied by Fourier transform infrared (FTIR) spectroscopy was obtain KBr pellets methodology (Perkin Elmer 1725 spectrometer, USA) in the wavenumber range of 400−4000 $cm^{-1}$. The morphology of the nanoparticles was observed by a field emission scanning microscope (FESEM) captured by FEI-Quanta FEG 200F (The Netherlands), equipped with an energy-dispersive X-ray (EDX) spectrum for elemental analysis and a 30 kV accelerating voltage. The transmission electron microscope (TEM) was performed with a JEOL/JEM 2100 (Japan) at a 200 kV accelerating voltage. To identify the sample's energy band, an optical characterization was done using a Cary 100 UV−visible spectrophotometer (USA) inside the 200−500 nm wavelength range using $BaSO_4$ as a reflectance sample.

**2.5. Evaluation of Antibacterial Activity.** Gram-positive as well as Gram-negative common pathogenic bacteria (*Staphylococcus aureus* (MTTC 3615), *Enterococcus faecalis* (MTCC 439), *Escherichia coli* (MTCC 443), and *Proteus mirabilis*) were selected for typical microorganisms for antibacterial screening (MTCC 1771). The growth of bacteria was accomplished using the Mueller−Hinton diffusion of agar disc technique. At first, the strains were cultivated using a standard cork borer method and by adjusting the turbidity of the bacterial inoculums. Fresh bacterial cultures were added to each well using a micropipette. Discs of 6 mm diameter containing the sample were dispensed onto the plates. The loaded plates were incubated at 37 °C for 24 h, the antibacterial activity was evaluated on the zone of diameter inhibition in mm, and the results were recorded. The test was repeated three times. A Vernier caliper was used to measure inhibition zones of the bacteria, and they were reordered for antibacterial activity.


https://doi.org/10.1021/acsomega.3c02432
ACS Omega 2023, 8, 38860−38870

**2.6. Antioxidant Activity.** *2.6.1. DPPH Radical Scavenging Assay.* Ag NPs and cellulose/Ag NPs were tested for their capacity to degrade free radicals using the DPPH (1, 1, diphenyl 2, 2, picrylhydrazyl) scavenging assay.[21,22] DPPH was used to evaluate the amounts of cellulose/Ag NPs (200−1000 g/mL). The following percentage (%) DPPH degradation properties for cellulose/Ag NPs were calculated: Scavenging ability of DPPH (%) = $[(A_{sample} - A_{blank})/A_{control}] \times 100$, where $A_{control}$ is the control absorbance at 30 min and $A_{sample}$ is the sample absorbance at 30 min. Each sample was examined in triplicate.

*2.6.2. $H_2O_2$ Radical Scavenging Assay.* The technique developed by Bhatti et al. was used to calculate the hydrogen peroxide scavenging capability of samples.[23] Ag NPs and cellulose/Ag NPs were generated in ethanol at varied concentrations (200−1000 g/mL) in 0.6 mL of $H_2O_2$ solution. The absorbance of the reaction mixture at 230 nm was measured at 15 min of incubation. A $H_2O_2$-only solution is referred to as a blank solution. The $H_2O_2$ scavenging activity of cellulose/Ag NPs was found to be as follows: (%) hydrogen peroxide scavenging = $[(A_o - A_1)/A_o] \times 100$, where $A_o$ seems to be the control absorbance and $A_1$ is the sample absorbance.

**2.7. Molecular Docking Studies.** *2.7.1. Protein Preparation.* In the current study, a molecular docking study for a protein connected to breast cancer research was conducted. The targeted crystalline structure of the BRCT replication originating from the penicillin-binding protein 4 (RCSB PDB ID: 1TVF), a protein linked with breast cancer, was retrieved and downloaded in the RCSB PDB format. All calculations of docking studies were carried out using the AutoDock-Vina program. The removal of cocrystallized ligands, fluids, and cofactors was done before the protein was ready for docking. The graphical user interface of Autodock tools (ADT) was employed to determine the Kollman charge and polar hydrogens. For the docking operation, AutoDock software's Lamarckian Genetic Algorithm (LGA) capability was used.

*2.7.2. Receptor Grid Generation.* Autodock 4.2 was used to perform molecular docking investigations. Studies of docking were conducted using stiff receptors and flexible ligands. At the binding site for the 1TVF protein, the grid box's dimensions were 126 × 126 × 126, and the grid box's center dimensions were −5.911 × 31.909 × 40.846, with a spacing of 0.389.

*2.7.3. Ligand Preparation.* The cellulose/Ag NP complexes' organic components were represented using ChemDraw 12.0 software. The generated 2D chemical structures were translated into the *mol* form that was later turned into the 3D AutoDock software's structure was used for the docking procedure, and all these ligands were subsequently purified and synthesized using Autodock ligand-input facilities via chosen torsional tree-choose roots as well as torsion tree-detect root. Using output-save, the purified finished ligands were saved in the *pdbqt* file for future use in molecular docking investigations. The visualization results were obtained using the Discovery Studio program.

**2.8. Photocatalytic Activity.** Photocatalytic performance was investigated using visible light (300 W xenon lamps; 400 nm). The photocatalytic efficiency of the as-prepared samples was determined at room temperature (RT). In a quartz glass photocatalytic reactor, exactly 200 mg of photocatalyst was disseminated into 100 mL of Rhodamine B (RhB) (10 mg/L). Before irradiation, the aliquot was agitated for 30 min in the dark to establish adsorption−desorption equilibrium between both dyes and the photocatalyst. UV absorption experiments were used to investigate the degradation efficiency and determine the dye concentrations at different time intervals.

## 3. RESULTS AND DISCUSSION

**3.1. Structural and Morphology Properties.** The crystallinity and crystal phases of green-synthesized Ag NPs and cellulose/Ag NPs were analyzed by XRD studies as shown in Figure 1a,b. In Ag NPs, a strong diffraction peak was

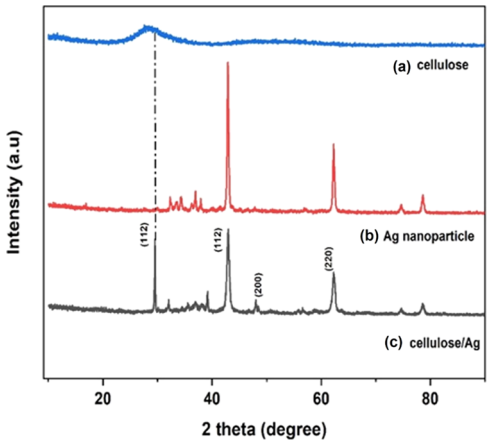


**Figure 1.** XRD patterns of (a) cellulose, (b) Ag NPs, and (c) cellulose/Ag NPs.

observed at 2$\theta$ values of 41.2, 47.3, and 64.4°, which correspond to (112), (200), and (220) planes, respectively, and all of these peaks are compatible with the face-centered cubic (fcc) phase of Ag NPs (JCPDS file no. 04-0783).[24,25] Further, we can see that common diffraction peaks of cellulose and Ag NPs appeared in the cellulose/Ag NPs (Figure 1); furthermore, strong diffraction peaks appeared at 41.2° having a large width, which represent the green-synthesized NPs having a small size compared to pure Ag NPs. Moreover, the cellulose peak (28°) intensity slightly increased in the cellulose/Ag NPs, implying the addition of Ag NPs into the cellulose matrix, which would help increase cellulose crystallinity and, further, help Ag NPs to diffuse into the cellulose crystalline region. A trend of increasing intensity of these peaks was observed when the Ag concentration was increased due to unreacted cellulose, emphasizing cellulose's beneficial role in stabilizing a distinct phase of the face-centered cubic structure of Ag NPs. As the concentration of Ag increases, the intensity of the cellulose XRD peaks increases dramatically. In the reaction solution, hydrogen bonds between adjacent cellulose molecules were likely induced by increased viscosity. A similar observation was made by Basuny et al. in the case of an increase in cellulose crystallinity in the cellulose/Ag composite.[26] The mean crystallite size of green-synthesized Ag NPs as well as the cellulose/Ag composite computed using the Debye−Scherrer equation[27] and the measured mean crystalline structure of silver nanoparticles were ∼32 and ∼24 nm, respectively.

The surface morphology, physical properties, and interfacial interaction of the green-synthesized Ag NPs and the cellulose/Ag NPs were observed through FESEM and TEM analyses. Figure 2a displays the sheet-like structure of the cellulose polymer matrix. Figure 2b shows the FESEM images of Ag NPs. It is noticed that the samples are spherical in nature and there is no agglomeration between the particles; furthermore, a


https://doi.org/10.1021/acsomega.3c02432
ACS Omega 2023, 8, 38860−38870

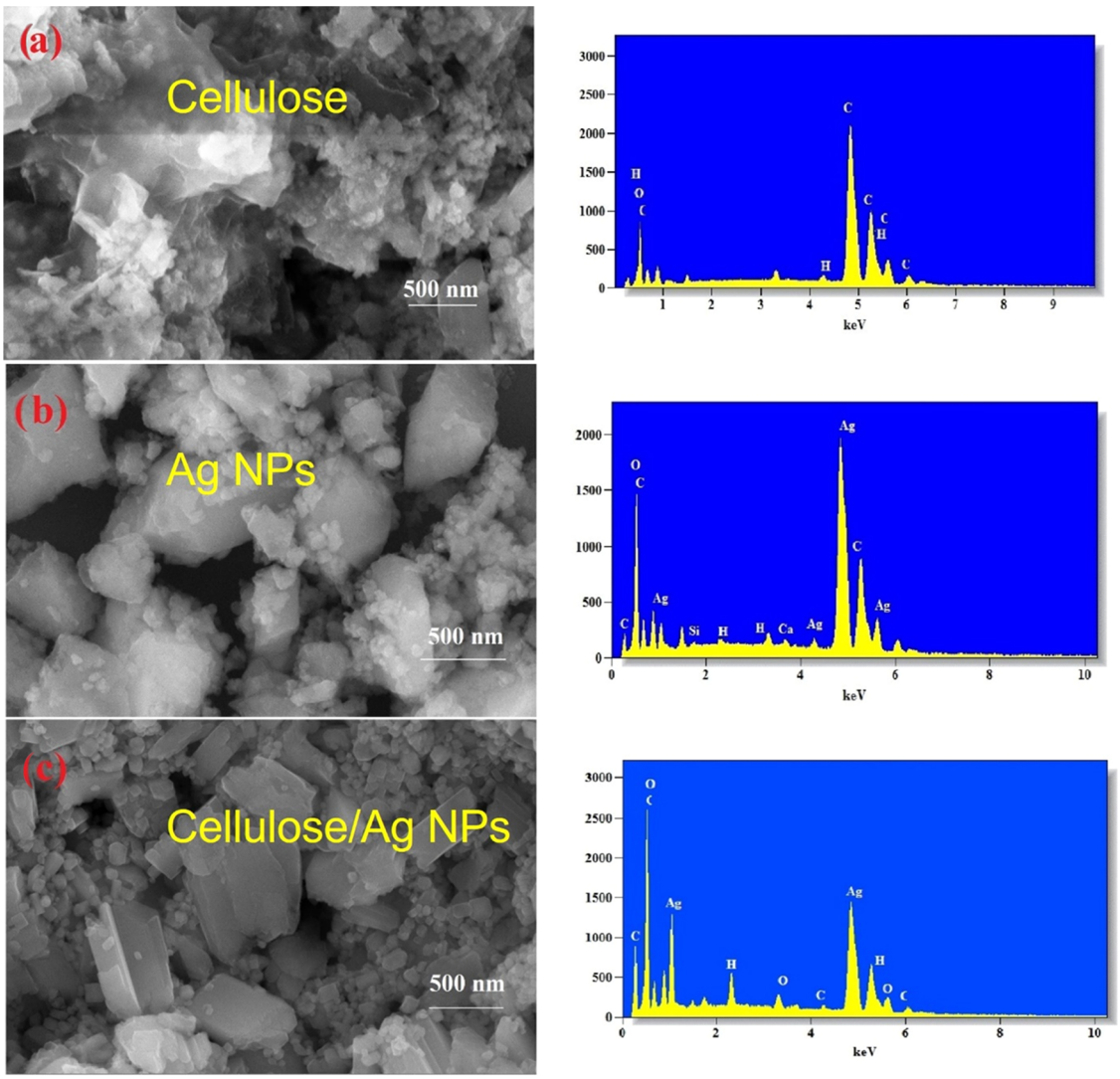


**Figure 2.** FESEM images of (a) cellulose, (b) Ag NPs, and (c) cellulose/Ag NPs and the respective EDX images.

large number of small chunks formed. FESEM images of Ag NPs and cellulose/Ag NPs showed a qualitatively small difference in the porous structure. Figure 2c shows the porous structure of cellulose/Ag NPs; a large number of spherical particles are observed along with fewer smaller chunks compared to pure Ag NPs, which indicate that the Ag NPs cause significant changes in the cellulose polymer matrix morphology. More interestingly, the cellulose/Ag NP architecture is induced by the interfacial interaction behavior between the cellulose matrix and Ag NPs during HPCM-assisted synthesis. The present study combines field-emission scanning electron microscopy (FESEM) with energy dispersive X-ray spectroscopy (EDX) analysis. X-ray spectroscopy (EDX) can offer valuable information regarding the elemental analysis of carbon, oxygen, and hydrogen related to the cellulose and silver was detected indicating the successful formation of the green-synthesized composite. TEM investigation was performed to verify the production of Ag NPs on the surface of the cellulose polymer matrix. Figure 3a reveals nanoparticles of Ag NPs via the HPCM route, while Figure 3b shows spherical-shaped Ag NPs present on the nanocluster of the cellulose polymer matrix surface and objects with size from several nm to 20 nm. The presence of available pores within the cellulose

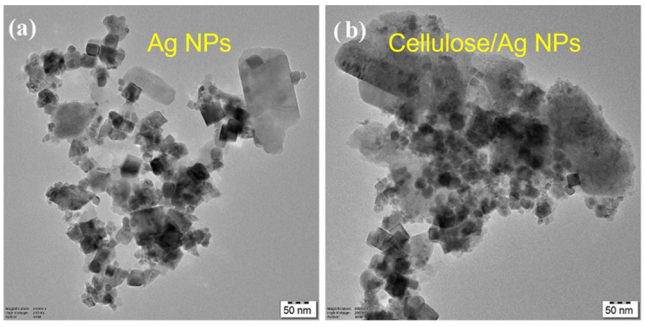


**Figure 3.** TEM images of (a) Ag NPs and (b) cellulose/Ag NPs.

matrix creates a growth site for embedded Ag NPs, leading to the smaller size of green-synthesized cellulose/Ag NPs in comparison to pure Ag NPs.

**3.2. FTIR Analysis.** FTIR spectra were used to examine both phytochemical constituents of cellulose, Ag NPs, and cellulose/Ag NPs as shown in Figure 4a,b. The spectra of cellulose showed a peak at 3169 and 1357 $cm^{-1}$ attributed to the O−H stretching vibration, and the band around 690 and 857 $cm^{-1}$ may be due to the COO stretch. The FTIR spectra of Ag NPs arise at 778 $cm^{-1}$ and 841 $cm^{-1}$, attributable to the



https://doi.org/10.1021/acsomega.3c02432
ACS Omega 2023, 8, 38860−38870

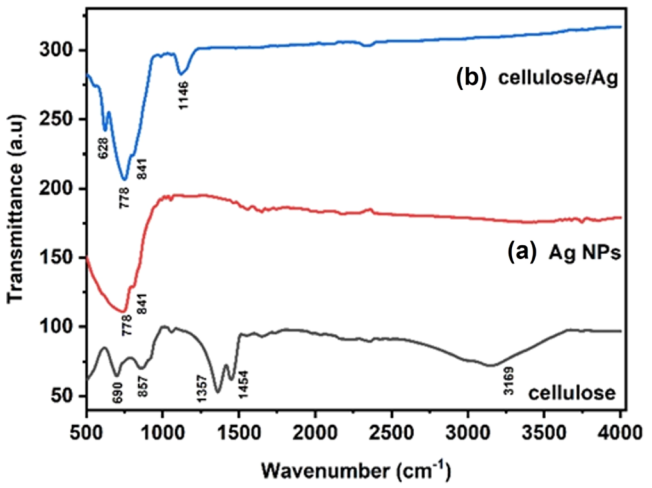


**Figure 4.** FTIR spectra of (a) Ag NPs and (b) cellulose/Ag NPs.

C═C stretching mode and C−H scissoring, respectively,[24,26] of the organic moisture. The FTIR spectra of cellulose/Ag NPs were obtained around 628, 778, 841, and 1146 $cm^{-1}$. For the composite, peaks around 628 and 1146 $cm^{-1}$ were linked to COO groups that signify carboxylate ion production during the production of cellulose/Ag NPs;[28] these peaks confirm the successful formation of cellulose/Ag NPs. Furthermore, the slight shift of the COO band from cellulose to the composite and the peak intensity increase from cellulose to the composite further confirm the formation of cellulose/Ag NPs. As can be seen from the picture, a characteristic absorption band was present at 3169 $cm^{-1}$ for cellulose and at 1357 $cm^{-1}$ for the O−H stretching vibration, respectively, on the FTIR spectrum of cellulose. The breakdown of some hydrogen bonds in the crystallinity index of cellulose/Ag NPs was explained by the complete decrease in the crystallinity index. It was confirmed by a decrease in the 3169 $cm^{-1}$ intensity and a shift of the 1357 $cm^{-1}$ intensity for the main hydroxyl group. As a result, the hydrogen-bonding bands of 3169 and 1357 $cm^{-1}$ of cellulose/Ag NPs disappeared along with the decrease in crystallinity. Overall, these findings are in agreement with the loss of the crystalline order observed via XRD on cellulose/Ag NPs.

**3.3. UV−Visible Measurements.** The UV−visible absorption spectrum was collected to confirm the surface plasmon resonance (SPR), which occurs due to the nanoparticle size effect in the coherent existence of free electrons in the conduction band (CB).[29,30] The samples of cellulose/Ag NPs and Ag NPs are shown in Figure 5a,b with their UV−visible spectra. The maximum absorption peak of Ag NPs was found at 380, 420, and 520 nm, and a clear blue shift in the cellulose/Ag NPs was noticed, which confirms the impregnation of silver NPs into the cellulose matrix as well as the successful formation of cellulose/Ag NPs. In fact, Vijayakumar

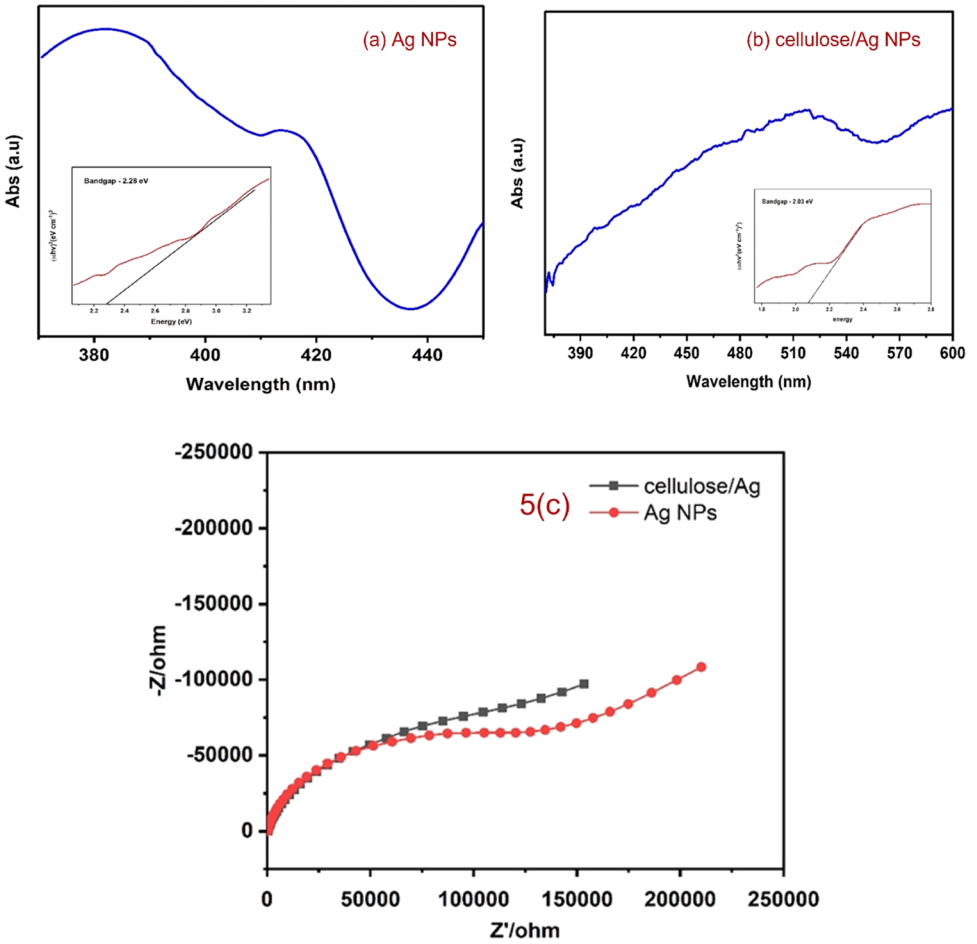


**Figure 5.** UV−visible spectrum of (a) Ag NPs and (b) cellulose/Ag NPs. (c). Charge transport properties and electrical conductivity of Ag NPs and cellulose/Ag NPs.



https://doi.org/10.1021/acsomega.3c02432
ACS Omega 2023, 8, 38860−38870

Table 1. Shape and Size of Cellulose/Ag Nanoparticles Affect their Antibacterial Efficiency

| organisms | streptomycin (mm) | antibacterial activity (mm) | | | | |
|---|---|---|---|---|---|---|
| | | 0.5 ($\mu$g/mL) | 1 ($\mu$g/mL) | 1.5 ($\mu$g/mL) | 2 ($\mu$g/mL) | 2.5 ($\mu$g/mL) |
| *Staphylococcus aureus* (MTTC 3615) | 20.1 ± 1.0 | 11.3 ± 0.5 | 12.7 ± 1.1 | 13.6 ± 0.5 | 14.8 ± 1.5 | 15.9 ± 0.5 |
| *Enterococcus faecalis* (MTCC 439) | 19.6 ± 0.5 | 13.3 ± 0.5 | 14.5 ± 0.5 | 15.2 ± 1.5 | 16.7 ± 1.1 | 17.7 ± 0.5 |
| *Escherichia coli* (MTCC 443) | 19.8 ± 1.0 | 11.6 ± 0.5 | 12.3 ± 0.5 | 14.3 ± 0.5 | 15.7 ± 1.1 | 17.4 ± 0.5 |
| *Proteus mirabilis* (MTCC 1771) | 20.1 ± 1.5 | 14.6 ± 1.5 | 15.2 ± 1.1 | 16.6 ± 0.5 | 17.9 ± 1.0 | 18.8 ± 1.5 |

et al.[28] reported that it should be noted that the observed SPR spectra intensity of the composite is due to the distribution of Ag NPs, spherical shape, and nanosize of the Ag NPs. The band gap of the specimens was determined using the Tauc plot $(\alpha h\nu)$ *vs* $C(h\nu - E_g)^n$, where $\nu$ is the intensity of light, $h$ represents Plank's constant, $C$ is the proportionality, $n$ represents 1/2 (for direct transition mode materials), and $E_g$ is the band-gap energy.[31] The band-gap energies of Ag NPs as well as cellulose/Ag NPs were 2.26 and 2.03 eV, respectively.

**3.4. Impedance Spectra.** Electrochemical impedance spectroscopy (EIS) measurement was carried out to investigate the charge transport features and degrees of electrical conductivity of Ag NPs and cellulose/Ag NPs. In Figure 5c, we can see a large semicircle arc, which indicates the high resistance of Ag NPs, and a small semicircle arc, which represents the low resistivity of cellulose/Ag NPs. Based on EIS results, cellulose/Ag NPs show a smaller semicircle radius in the EIS plot, suggesting a lower interfacial layer resistance to a faster interfacial transfer of the electron−hole $(e^-/h^+)$ pair.[32−34] The results indicated that the cellulose strongly coupled with Ag NPs facilitates electron−hole transfer and migration, which supports the better antibacterial and photocatalytic activities of cellulose/Ag NPs.

**3.5. Antibacterial Activity.** Using the disc-diffusion technique, the antibacterial capabilities of Ag NPs and cellulose/Ag NPs were investigated against both Gram-positive and Gram-negative bacteria. The antibacterial assay result of cellulose/Ag NPs is collated in Table 1 and is shown in Figure 6, which states that cellulose/Ag NPs produce a good

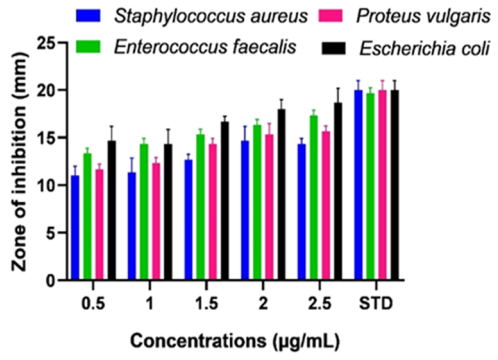


**Figure 6.** Antibacterial activity of cellulose/Ag NPs against *S. aureus*, *P. vulgaris*, *E. faecalis*, and *E.coli*.

inhibition zone against both bacteria. This test demonstrates that pure Ag NPs showed the lowest inhibition effect on both tested bacteria when compared with cellulose/Ag NPs, and the results showed marked suppression against Gram-negative bacteria than against Gram-positive bacteria. The antibacterial activity of cellulose/Ag NPs was different against human pathogens due to differences in the cell membranes of Gram-positive and Gram-negative cells. Gram-positive bacterial cell walls are made of a single peptidoglycan layer. Thus, cellulose/Ag NPs could easily penetrate Gram-positive bacteria. However, the Gram-negative bacterial cell wall is a multilayered structure, which contains a lipoprotein layer, a phospholipid layer, and a thin peptidoglycan layer,[17] so penetration of cellulose/Ag NPs into the Gram-negative bacteria was prevented by their complex structure. The possible mechanism of the antibacterial effect of the cellulose/Ag NPs is summarized in Figure S1.

The mechanism of cellulose/Ag NPs' antibacterial effectiveness has been postulated.

(i) The antibacterial efficiency of the synthesized cellulose/Ag NPs depends on the shape and size of the nanoparticles. The small-sized nanoparticles became more toxic than the large nanoparticles due to their higher surface-to-volume ratio. Therefore, small nanoparticles help it to penetrate into the cell easily, which leads to bacterial effects in the bacterial species.[17]

(ii) Another potential method of action includes membrane function; metallic nanoparticles have a positively charged surface that allows them to interact with negatively charged bacterium membranes, enabling them to attach to various cell structures and leading to chemical interaction. The electrostatic interaction occurs between positively charged metallic nanoparticles and negatively charged bacteria on the surface and charged in cell morphology, leading to growth inhibition.[35]

(iii) ROS are a species of oxygen that can damage the cell membrane, DNA, and cellular protein, which leads to cell death.[36,37] ROS are produced when oxygen enters undersized reduction states, which may be attributed to the formation of oxidative stress by the superoxide anion $(O_2^{\bullet -})$, hydrogen peroxide $(H_2O_2)$, and the hydroxide radical $(OH^{\bullet})$, which leads to the formation of $H_2O_2$ and further damages the DNA as well as proteins in bacteria.

**3.6. Antioxidant Activity.** *3.6.1. DPPH Radical Scavenging Activity.* Cellulose/Ag NPs from the green synthesis show profound free-radical scavenging activity against DPPH as shown in Figure 7a. The cellulose/Ag NPs demonstrate high antioxidant activity compared to *I. quamoclit* extract Ag NPs and are well-known ascorbic acid antioxidants. In this study, the DPPH degradation capabilities of cellulose/Ag NPs significantly increased in a dose-dependent manner. Functional cellulose/Ag NPs exhibited maximum DPPH scavenging traits ranging from 24.5 ± 0.6 to 77.2 ± 4.0% for the ascorbic acid standard. The obtained result might be attributed to the presence of various phytochemical groups, as shown in the FTIR, which was a reason for the reduction of Ag NPs to cellulose/NPs.

*3.6.2. $H_2O_2$ Scavenging Activity.* Hydrogen peroxide is known as the primary reactive oxygen species (ROS) due to its biological properties. The hydrogen peroxide radical scaveng-


https://doi.org/10.1021/acsomega.3c02432
ACS Omega 2023, 8, 38860−38870

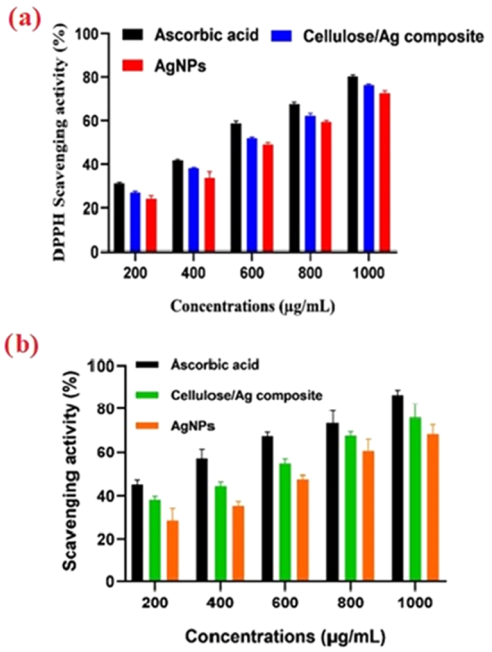


**Figure 7.** (a). DPPH scavenging effect of different concentrations (200−1000 $\mu$g/mL) of Ag NPs, cellulose/Ag NPs, and ascorbic acid. Each value represents the mean ± standard error of the mean (SEM) of triplicate experiments. (b). $H_2O_2$ degrading properties of Ag NPs and cellulose/Ag NPs at various concentrations (200−1000 $\mu$g/mL).

ing properties of the Ag NPs and cellulose/Ag NPs with the standard are shown in Figure 7b. The functional cellulose/Ag NPs showed maximum $H_2O_2$ scavenging traits ranging from 39.1 ± 1.6 to 79.8 ± 6.1% and standard ascorbic acid ranging between 45.1 ± 2.1 and 88.5 ± 2.1%; based on the findings, functional cellulose/Ag NPs showed stronger concentration-dependent antioxidant activities.

**3.7. Studies on Molecular Docking.** *3.7.1. Molecular Docking Studies of Cellulose/Ag NP Ligand with the Crystal Structure of (PDB ID: 1TVF) the Penicillin-Binding Protein 4 (PBP4) from Staphylococcus aureus.* At least a dozen different proteins work together to control the complicated processes of bacterial cell division, including daughter cell formation. For more than 70 years, $\beta$-lactam antibiotics have been utilized as the targets for penicillin-binding proteins (PBPs) and membrane-associated macromolecules, which are required for cell wall synthesis. The increasing frequency of $\beta$-lactam-resistant microorganisms and the advances made in genomics, genetics, and immunofluorescence microscopy procedures have motivated extensive investigation into PBPs from a variety of bacterial taxa. Additionally, a recent publication of the high-resolution structure for PBPs from pathogenic species has shed light on the complex relationship between drug-resistant and cell division processes.

The binding affinities and inhibition constants $K_i$ of all produced ligands are shown in Table S1. Table S2 reveals that all of the cellulose/Ag ligands could robustly occupy the active site of 1TVF, with their residue interactions, bond types, and bond lengths. The pictures of cellulose/Ag NPs with ligand−receptor hydrogen-bond contacts, receptor-side hydrogen-bonding interaction, and associated 2D ligand−receptor hydrogen-bond interactions are shown in Figures 8,9, and 10 as well as in Figure S2. For four distinct receptors, empirical ligand binding energy levels with their respective RMSD measurements (rmsd l.b and rmsd u.b) were provided. The inhibitory factors for all compounds were calculated and reported using the $K_i = \exp(\Delta G/RT)$ equation, where $\Delta G$, $R$, and $T$ are the docking binding energy, gas constant (1.9872036 × $10^{-3}$ kcal/mol), and temperature (298.15 K), respectively. An inhibition constant ($K_i$) shows that whenever a ligand had stopped associating with such a material for the enzyme and serves as a measure of ligand binding to protein. The smaller the $K_i$, the lesser the drug necessary to inhibit the enzyme's activity. The cellulose/Ag NP ligands interact with the 1TVF protein, resulting in a decreased $\Delta d$ binding affinity of −5.8 (kcal/mol) as well as an inhibitory constant ($K_i$) of 55.444 M.

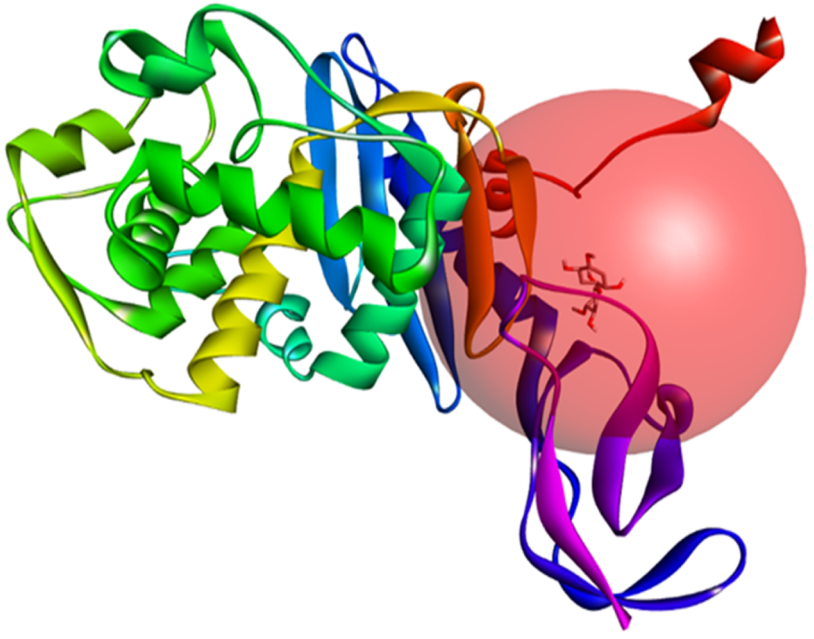

**Figure 8.** Receptor 1TVF and cellulose/Ag ligand active-side prediction binding image outcome.



https://doi.org/10.1021/acsomega.3c02432
ACS Omega 2023, 8, 38860−38870

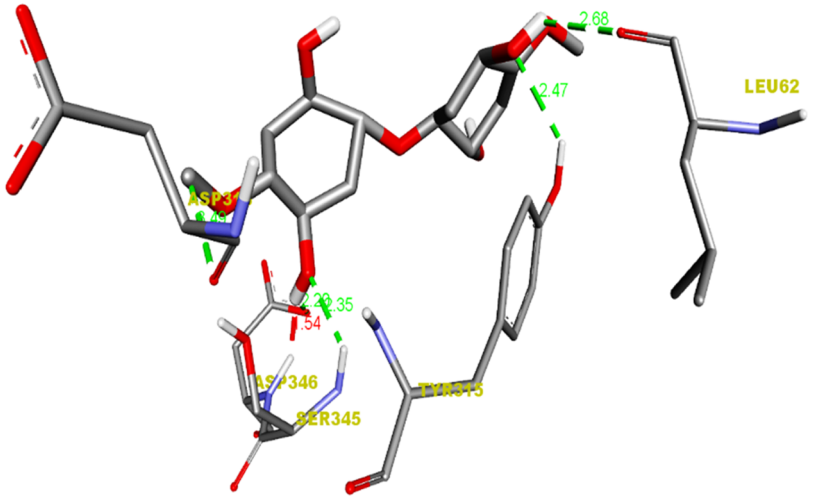


**Figure 9.** Hydrogen-bond Interaction of the cellulose/Ag ligand with the 1TVF protein.

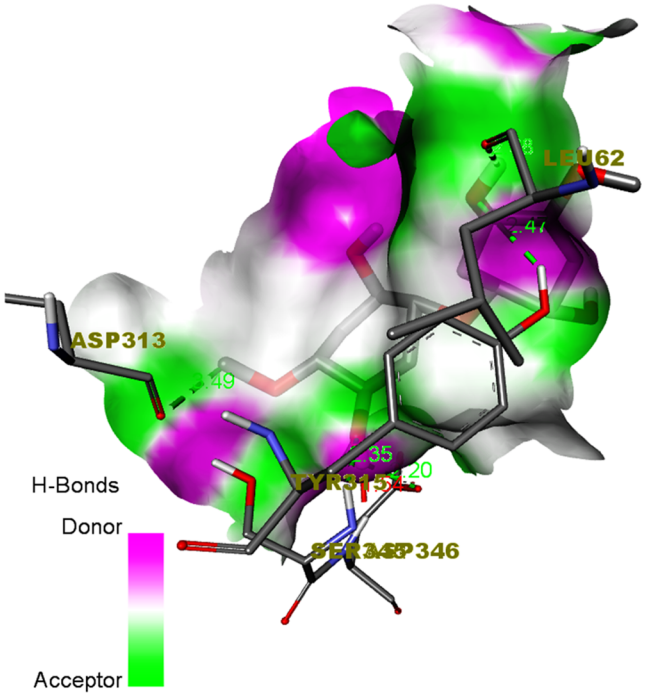


**Figure 10.** Hydrogen-bond receptor-side surface interaction of the cellulose/Ag ligand with the 1TVF protein.

**3.8. Photocatalytic Activity.** In order to create a photocatalyst, the adsorption−desorption equilibrium was obtained in 30 min and the photocatalytic destruction of RhB under exposure to visible light was investigated. Figure 11a shows the photocatalytic degradation efficiency of $C/C_o$ (%) vs time for RhB. After 180 min, the photocatalytic activity of a blank solution was tested in the absence of a photocatalyst; the result shows that the degradation rate is around 7.37%. The degradation performances of the RhB solution utilizing Ag NPs and cellulose/Ag NPs were found to be 37.68 and 97.38%, respectively. The UV-adsorption intensity for RhB rapidly reduced as the reaction time increased as shown in Table S3.

*3.8.1. Kinetic Study of Reactions.* A pseudo-first-order equation may be used to depict the kinetic rate of cellulose/Ag nanoparticles against RhB dye degradation.

$$-\ln(C_t/C_o) = k_{abs}(t) \quad (1)$$

where $C_t$ is the concentration for RhB at different time intervals ($t$), $C_o$ is the starting dye concentration, and $k_{abs}$ is the pseudo-first-order model constant of dye removal. Figure 11b shows the cellulose/Ag rate constant, which aids in the photocatalytic breakdown of RhB. Table S4 illustrates the constant $k_{abs}$ values of RhB derived from experimental data.

*3.8.2. Mechanism for Photocatalysis.* From the experimental results and comments illustrated in Figure 12, cellulose/Ag NPs can be used as photocatalysts to degrade RhB. When visible light is absorbed on the surface of NPs, electrons are pushed from the valence band (VB) to the conduction band (CB) while creating holes ($h^+$) in the VB. During this process, the rate of electron−hole pairs decreases, which improves the photocatalytic process. The CB electron reacts with the dissolved oxygen molecules to result in peroxide radical anions ($^{\bullet}O_2^-$), and the interaction between holes and $OH^-$ ions produces hydroxyl radicals ($^{\bullet}OH$). In the vicinity of $^{\bullet}OH$ as well as $^{\bullet}O_2^-$ species, the RhB disintegrates, generating $CO_2$ and $H_2O$.[38,39] The equation specifies the suitable photocatalytic degradation pathway.

$$\text{cellulose/Ag} + \text{visible light } (h\nu) \rightarrow h^+ (\text{VB}) + e^- (\text{CB}) \quad (2)$$

$$h^+ (\text{VB}) + H_2O \rightarrow H^+ + {}^{\bullet}OH \quad (3)$$

$$e^- + O_2 \rightarrow {}^{\bullet}O_2^- \quad (4)$$

$$[\text{RhB dye}] + {}^{\bullet}O_2^- + {}^{\bullet}OH \rightarrow H_2O + CO_2 \quad (5)$$

## 4. CONCLUSIONS

The present work demonstrates cellulose/Ag nanoparticles were successfully prepared by a simple, eco-friendly, and economical hydrothermal technique. XRD, FTIR, FESEM, TEM, and UV−visible spectroscopy were used to investigate the structural, morphological, and optical features of green-synthesized Ag NPs and cellulose/Ag NPs. The XRD analysis revealed that the samples were crystalline in nature with an *fcc* structure, and Ag ions were successfully incorporated in the cellulose polymer matrix. FESEM and TEM analyses indicated that the green-synthesized cellulose/Ag NPs were spherical in shape, with the Ag NPs securely adhered to the cellulose


https://doi.org/10.1021/acsomega.3c02432
ACS Omega 2023, 8, 38860−38870

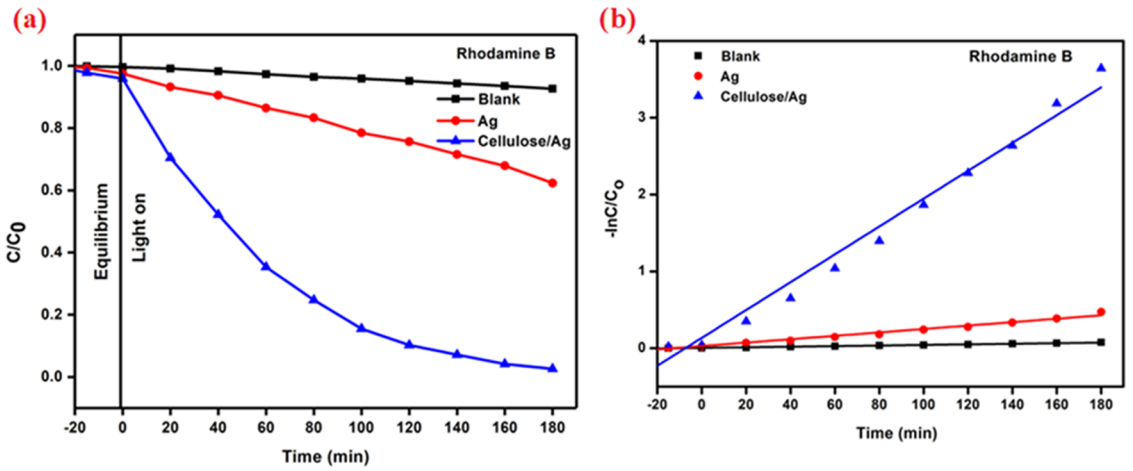


**Figure 11.** (a) $C/C_o$ versus time for Rhodamine B dye degradation. (b) Kinetic plot for Rhodamine B.

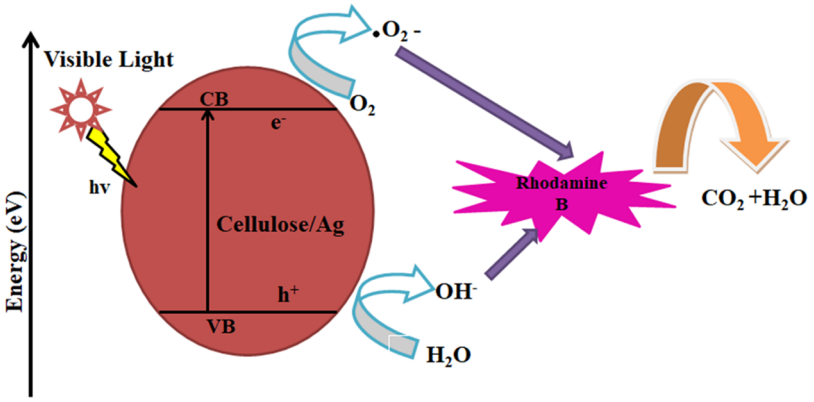


**Figure 12.** Photocatalytic activity mechanism of cellulose/Ag NPs against RhB.

surface. The UV−visible spectra demonstrate the production of cellulose/Ag NPs by SRP peaks approximately at 520 nm. As compared to both manufactured Ag NPs as well as cellulose/Ag NPs, these cellulose/Ag NPs demonstrated considerable antibacterial activity against Gram-positive bacteria but not against Gram-negative bacteria. In addition, cellulose/Ag composites may have potential antioxidant properties when compared to Ag nanoparticles.s. Additionally, at the completion of 180 min of UV−visible irradiation, the cellulose/Ag NP sample showed a higher degradation efficiency compared to pure Ag NPs against Rhodamine B as 97.38% removal was achieved. This research provides an environmentally friendly and simple method for cellulose/Ag NPs to be further applied in the field of functional biomedical applications, which needs to be further investigated in further studies.

## ■ ASSOCIATED CONTENT

### Supporting Information

The Supporting Information is available free of charge at https://pubs.acs.org/doi/10.1021/acsomega.3c02432.

Preparation of the materials, mechanism of antibacterial activity, and representation of the 2D hydrogen-bond interaction between the cellulose/Ag ligand and the 1TVF protein, mechanism of photocatalytic activity of cellulose/Ag NPs against RhB, analysis of the binding affinity and RMSD values of different poses in 1TVF inhibitors of cellulose/Ag NP compounds, Rhodamine B degradation into cellulose/Ag based on the ligand−receptor interaction between the cellulose/Ag ligand and the 1TVF protein; and the value for the rate constant of Rhodamine B degradation on cellulose/Ag (PDF)

## ■ AUTHOR INFORMATION

### Corresponding Authors

**Arularasu M. Visagamani** − *Department of Electronic Engineering, Chang Gung University, Taoyuan 33302, Taiwan;* orcid.org/0000-0001-9969-2112; Email: arulrs597@gmail.com

**Kasinathan Kaviyarasu** − *UNESCO-UNISA Africa Chair in Nanosciences/Nanotechnology Laboratories, College of Graduate Studies, University of South Africa (UNISA), Pretoria 0002, South Africa; Nanosciences African Network (NANOAFNET), Materials Research Group (MRG), iThemba LABS−National Research Foundation (NRF), Somerset West 7129 Western Cape, South Africa;* Email: kavi@tlabs.ac.za

### Authors

**Durairaj Shanthi** − *Department of Chemistry, VelTech MultiTech Dr. Rangarajan Dr. Sakunthala Engineering College, Chennai 600062, India*

**Appusamy Muthukrishnaraj** − *Department of Chemistry, Faculty of Engineering, Karpagam Academy of Higher Education, Coimbatore 641021 Tamil Nadu, India*



https://doi.org/10.1021/acsomega.3c02432
ACS Omega 2023, 8, 38860−38870

**Babu Venkatadri** − *Department of Biomedical Science and Environmental Biology, Kaohsiung Medical University, Kaohsiung 80708 Taiwan, ROC*

**J. Irshad Ahamed** − *Department of Chemistry, Kandaswami Naidu College for Men, Chennai 600102, India*

Complete contact information is available at: https://pubs.acs.org/10.1021/acsomega.3c02432

### Funding

The authors declare that they do not have any competing financial interests or personal relationships that could influence the findings.

### Notes

The authors declare no competing financial interest.

## ■ ACKNOWLEDGMENTS

The authors acknowledge and appreciate the management for its support and encouragement.

## ■ REFERENCES

(1) Slavin, Y. N.; Asnis, J.; Hafeli, U. O.; Bach, H. Metal nanoparticles: understanding the mechanisms behind antibacterial activity. *J. Nanobiotechnol.* **2017**, *15*, No. 65.

(2) Doan Thi, T. U.; Nguyen, T. T.; Thi, Y. D.; Ta Thi, K. H.; Phanbc, B. T.; Pham, K. N. Green synthesis of ZnO nanoparticles using orange fruit peel extract for antibacterial activities. *RSC Adv.* **2020**, *10*, 23899.

(3) Arularasu, M. V.; Devakumar, J.; Rajendran, T. V. An innovation approach for green synthesis of iron oxide nanoparticles: characterization and its photocatalytic activity. *Polyhedron* **2018**, *156*, 279−290.

(4) Regiel-Futyra, A.; Kus-Liskiewicz, M.; Sebastian, V.; Irusta, S.; Arruebo, M.; Stochel, G.; Kyziol, A. Development of noncytotoxic chitosan−gold nanocomposites as efficient antibacterial materials. *ACS Appl. Mater. Interfaces* **2015**, *7*, 1087−1099.

(5) Jeon, Y.; Nagappan, S.; Xi-Hui, L.; Joon-Hee, L.; Shi, L.; Yuan, S.; Won-Ki, L.; Chang-Sik, H. Highly transparent, robust hydrophobic, and amphiphilic organic−inorganic hybrid coatings for antifogging and antibacterial applications. *ACS Appl. Mater. Interfaces* **2021**, *13*, 6615−6630.

(6) Anusa, R.; Ravichandran, C.; Rajendran, T. V.; Arularasu, M. V.; Sivakumar, E. K. T. Comparative investigation of cobalt ferrite ($CoFe_2O_4$) and cadmium ferrite ($CdFe_2O_4$) nanoparticles for the structural, optical properties and antibacterial activity. *Dig. J. Nanomater. Biostruct.* **2019**, *14*, 367−374.

(7) Shi, L. E.; Li, Z. H.; Zheng, W.; Zhao, Y. F.; Jin, Y. F.; Tang, Z. X. Synthesis, antibacterial activity, antibacterial mechanism and food applications of ZnO nanoparticles: a review. *Food Addit. Contam.: Part A* **2013**, *31*, 173−186.

(8) Hasan Mujahid, M.; Kumar Upadhyay, T.; Khan Pratibha, F.; Moon Nyeo, P.; Amit Baran Sharangi, P.; Saeed, M.; Upadhye, V. J.; Kim, B. Metallic and metal oxide-derived nanohybrid as a tool for biomedical applications. *Biomed. Pharmacother.* **2022**, *155*, No. 113791.

(9) Li, J.; Cha, R.; Mou, K.; Zhao, X.; Long, K.; Luo, H.; Zhou, F.; Jiang, X. Nanocellulose-based antibacterial materials. *Adv. Healthcare Mater.* **2018**, *7*, No. 1800334.

(10) Aryan, R.; Singh Mehata, M. Green synthesis of silver nanoparticles using Kalanchoe pinnata leaves (life plant) and their antibacterial and photocatalytic activities. *Chem. Phys. Lett.* **2021**, *778*, No. 138760.

(11) Hasnain, M. S.; Javed, M. N.; Alam, M. S.; Rishishwar, P.; Rishishwar, S.; Ali, S.; Kumar Nayak, A.; Beg, S. Purple heart plant leaves extract-mediated silver nanoparticle synthesis: Optimization by Box-Behnken design. *Mater. Sci. Eng., C* **2019**, *99*, 1105.

(12) Maria Magdalane, C.; Kaviyarasu, K.; Raja, A.; Arularasu, M. V.; Mola, G. T.; Isaev, A. B.; Al-Dhabi, N. A.; Arasu, M. V.; Jeyaraj, B.; Kennedy, J.; Maaza, M. Photocatalytic decomposition effect of erbium doped cerium oxide nanostructures driven by visible light irradiation: Investigation of cytotoxicity, antibacterial growth inhibition using catalyst. *J. Photochem. Photobiol., B* **2018**, *185*, 275−282.

(13) Ehsan, M.; Yazdi, T.; Darroudi, M.; Sadegh Amiri, M.; Ali Hosseini, H.; Nourbakhsh, F.; Mashreghi, M.; Farjadi, M.; Mousa Mousavi Kouhi, S.; Hadi Mousavi, S. Anticancer, antimicrobial, and dye degradation activity of biosynthesised silver nanoparticles using Artemisa konetdaahensis. *Micro Nano Lett.* **2020**, *15*, 1046−1050.

(14) An, S.; Jeona, B.; Hyuk Baeb, J.; Soo Kimd, I.; Paenge, K.; Kima, M.; Lee, H. Thiol-based chemistry as versatile routes for the effective functionalization of cellulose nanofibers. *Carbohydr. Polym.* **2019**, *226*, 115259−115267.

(15) Rotaru, R.; Savin, M.; Tudorachi, N.; Peptu, C.; Samoila, P.; Sacarescu, L.; Harabagiu, V. Ferromagnetic iron oxide−cellulose nanocomposites prepared by ultrasonication. *Polym. Chem.* **2018**, *9*, 860−868.

(16) Joram Mendozaa, D.; Brownea, C.; Singh Raghuwanshia, V.; Simonb, G. P.; Garnier, G. One-shot TEMPO-periodate oxidation of native cellulose. *Carbohydr. Polym.* **2019**, *226*, No. 115292.

(17) Arularasu, M. V.; Harb, M.; Sundaram, R. Synthesis and characterization of cellulose/$TiO_2$ nanocomposite: Evaluation of in vitro and in silico molecular docking studies. *Carbohydr. Polym.* **2020**, *249*, No. 116868.

(18) Meng, C.; Hu, J.; Gourlay, K.; Yu, C.; Saddler, J. N. Controllable synthesis uniform spherical bacterial cellulose and their potential applications. *Cellulose* **2019**, *26*, 8325.

(19) Farooq, A.; Kayes Patoary, M.; Zhang, M.; Mussana, H.; Li, M.; Awais Naeem, M.; Mushtaq, M.; Farooq, A.; Liu, L. Cellulose from sources to nanocellulose and an overview of synthesis and properties of nanocellulose/zinc oxide nanocomposite materials. *Int. J. Biol. Macromol.* **2020**, *154*, 1050.

(20) Wang, W.; Zhang, B.; Jiang, S.; Bai, H.; Zhang, S. Use of $CeO_2$ nanoparticles to enhance UV-shielding of transparent regenerated cellulose films. *Polymers* **2019**, *11*, 458.

(21) Babu, V.; Arokiyaraj, S.; Pon Sakthi Sri, S.; George, M.; Marimuthu Ragavan, R.; Dharmalingam, D.; Oh, T.; Ramasundaram, S.; Agastian, P. Antibacterial, Antioxidant, Larvicidal and Anticancer Activities of Silver Nanoparticles Synthesized Using Extracts from Fruits of *Lagerstroemia speciose* and Flowers of *Couroupita guianensis*. *Molecules* **2022**, *27*, 7792.

(22) Irshad Ahamed, J.; Francy, K.; Priya, V.; PremaKumari, J.; Steiny, R. P.; Kamalarajan, P.; Venkatadri, B. Computational and biological efficacy of stigmasterol against HeLa cells and Vero cells-first time isolated from the ethanolic extract of Annonamuricata Linn leaves. *J. Mol. Struct.* **2022**, *1252*, No. 132186.

(23) Bhatti, M. Z.; Ali, A.; Ahmad, A.; Saeed, A.; Akbar Malik, S. Antioxidant and phytochemical analysis of Ranunculus arvensis L. extracts. *BMC Res. Notes* **2015**, *8*, 279.

(24) Parthiban, E.; Manivannan, N.; Ramanibai, R.; Mathivanan, N. Green synthesis of silver-nanoparticles from Annona reticulata leaves aqueous extract and its mosquito larvicidal and anti-microbial activity on human pathogens. *Biotechnol. Rep.* **2019**, *21*, No. e00297.

(25) Oliveira, J. P. d.; Bruni, G. P.; Lima, K. O.; Halal, S.; Rosa, G.; Dias, A.; Zavareze, E. Cellulose fibers extracted from rice and oat husks and their application in hydrogel. *Food Chem.* **2017**, *221*, 153−160.

(26) Basuny, M.; Ali, I. O.; El-Gawad, A. A.; Bakr, M. F.; Salama, T. M. A fast green synthesis of Ag nanoparticles in carboxymethyl cellulose (CMC) through UV irradiation technique for antibacterial applications. *J. Sol-Gel Sci. Technol.* **2015**, *75*, 530−540.

(27) Firdous, A.; Aslam Baba, M.; Singh, D.; Hamid Bhat, A. Optical and impedance studies of pure and Ba-doped ZnS quantum dots. *Appl. Nanosci.* **2015**, *5*, 201−206.

(28) Vijayakumar, S.; Chen, J.; Amarnath, M.; Tungare, K.; Bhori, M.; Divya, M.; Gonzalez Sanchez, Z. I.; Durán-Lara, E. F.; Vaseeharan, B. Cytotoxicity, phytotoxicity, and photocatalytic assessment of biopolymer cellulose-mediated silver nanoparticles. *Colloids Surf., A* **2021**, *628*, No. 127270.

(29) Fadakar Sarkandi, A.; Montazer, M.; Harifi, T.; Mahmoudi Rad, M. Innovative preparation of bacterial cellulose/silver nanocomposite hydrogels: In situ green synthesis, characterization, and antibacterial properties. *J. Appl. Polym. Sci.* **2021**, *138*, No. e49824.
(30) Li, J.; Kang, L.; Wang, B.; Chen, K.; Tian, X.; Ge, Z.; Zeng, J.; Xu, J.; Gao, W. Controlled release and long-term antibacterial activity of dialdehyde nanofibrillated cellulose/silver nanoparticle composites. *ACS Sustainable Chem. Eng.* **2019**, *7*, 1146−1158.
(31) Muthulakshmi, L.; Rajini, N.; Varada Rajalu, A.; Siengchin, S.; Kathiresan, T. Synthesis and characterization of cellulose/silver nanocomposites from bioflocculant reducing agent. *Int. J. Biol. Macromol.* **2017**, *103*, 1113−1120.
(32) Huang, Y.; Guo, Z.; Liu, H.; Zhang, S.; Wang, P.; Lu, J.; Tong, Y. Heterojunction architecture of N-doped $WO_3$ nanobundles with $Ce_2S_2$ nanodots hybridized on a carbon textile enables a highly efficient flexible photocatalyst. *Adv. Funct. Mater.* **2019**, *29*, No. 1903490.
(33) Li, Y.; Xia, Y.; Liu, K.; Ye, K.; Wang, Q.; Zhang, S.; Huang, Y.; Liu, H. Constructing Fe-MOF-derived Z-scheme photocatalysts with enhanced charge transport: nanointerface and carbon sheath synergistic effect. *ACS Appl. Mater. Interfaces* **2020**, *12*, 25494−25502.
(34) Zou, H.; Li, G.; Duanb, L.; Koua, Z.; Wangd, J. In situ coupled amorphous cobalt nitride with nitrogen-doped graphene aerogel as a trifunctional electrocatalyst towards Zn-air battery deriven full water splitting. *Appl. Catal., B* **2019**, *259*, No. 118100.
(35) Kuyukina, M. S.; Makarova, M. V.; Pistsova, O. N.; Glebov, G. G.; Osipenko, M. A.; Ivshina, I. B. Exposure to metal nanoparticles changes zeta potentials of Rhodococcus cells. *Heliyon* **2022**, *8*, No. e11632.
(36) Checa, J.; Aran, J. M. Reactive oxygen species: drivers of physiological and pathological processes. *J. Inflamm. Res.* **2020**, *13*, 1057−1073.
(37) Zhang, C.; Wang, X.; Du, J.; Gu, Z.; Zhao, Y. Reactive oxygen species-regulating strategies based on nanomaterials for disease treatment. *Adv. Sci.* **2021**, *8*, No. 2002797.
(38) Li, K.; Lua, X.; Zhanga, Y.; Liua, K.; Huanga, Y.; Liu, H. $Bi_3TaO_7/Ti_3C_2$ heterojunctions for enhanced photocatalytic removal of water-borne contaminants. *Environ. Res.* **2020**, *185*, No. 109409.
(39) Huang, Y.; Fan, W.; Long, B.; Li, H.; Zhao, F.; Liu, Z.; Tong, Y.; Ji, H. Visible Light $Bi_2S_3/Bi_2O_3/Bi_2O_2CO_3$ Photocatalyst for Effective Degradation of Organic Pollutions. *Appl. Catal., B* **2016**, *185*, 68−76.


https://doi.org/10.1021/acsomega.3c02432
*ACS Omega* 2023, 8, 38860−38870